Supplementary Information for:

Physics-based model reconciles caldera collapse induced static and dynamic ground motion: application to Kīlauea 2018

Taiyi Wang[1], Katherine Coppess[2], Paul Segall[1], Eric M. Dunham[1,3], William Ellsworth[1]

[1]Department of Geophysics, Stanford University
[2]Department of Physics, Stanford University
[3]Institute of Computational and Mathematical Engineering, Stanford University

1 Energy balance for the lumped parameter model

The mechanical energy balance can be derived directly from the momentum balance. First multiply both sides of the momentum balance with piston velocity, $\dot{u}$:

$$\dot{u}(m'\ddot{u} + \frac{\pi^2 R^4}{\beta V}u) = \dot{u}(mg - (2\pi RL)\tau - (\pi R^2)p_0) \tag{1}$$

which can be written as:

$$\frac{\partial}{\partial t}(\frac{1}{2}m'\dot{u}^2) = \frac{\partial}{\partial t}(mgu) - [\frac{\pi^2 R^4}{\beta V}\frac{\partial}{\partial t}(\frac{u^2}{2}) + \pi R^2 p_0 \frac{\partial u}{\partial t}] - (2\pi RL)\tau\frac{\partial u}{\partial t} \tag{2}$$

The above expression has dimensions of energy per unit time. The terms on the left hand side correspond to rate of change in piston kinetic energy. The terms on the right hand side correspond to rate of change in gravitational potential, rate of change in elastic strain energy of chamber + internal energy of magma, and work done against friction, respectively. Integrate both sides in time to get mechanical energy balance:

$$mg\Delta u - [\frac{1}{2}\Delta u^2\frac{\pi^2 R^4}{\beta V} + (\pi R^2)p_0\Delta u] - (2\pi RL)\tau_d\Delta u = 0 \tag{3}$$

Note kinetic energy term vanishes because piston velocity is at equilibrium at the beginning and end of the integration. Radiated energy and fracture energy are not included in this analysis, as discussed in the main text.

2 Sensitivity of simulated waveforms to model parameters

The simulated waveforms are sensitive to variations in each inverted parameters (Fig. S1). Notably, within a physically plausible range of parameter values, the simulated waveforms are highly sensitive to shear strength drop, $\Delta\tau_{str}$, total compressibility, β, effective magma density, $\phi\rho_f$, and piston radius, R. The apparent lack of sensitivity to chamber volume, V, chamber aspect ratio, α, and piston density, ρ_p, is due to the relatively small variations in parameter values (within one order of magnitude), as expected in nature. Note the relative lack of sensitivity to chamber aspect ratio in the waveforms is partially compensated by the high sensitivity of near-field static displacement to aspect ratios.

The dependence of waveform characteristics on each parameter can also be deduced from scaling relationships (Eqn. 9a, 9b, B1a-c, B2b in main text). For example, the increase of waveform duration with β, $\phi\rho_f$ correspond to longer characteristic time, t^*. Increase $\Delta\tau_{str}$ increases $F_{z,max}$, resulting in larger peak amplitude of velocity waveforms.

Corresponding author: Taiyi Wang, taiyi@stanford.edu

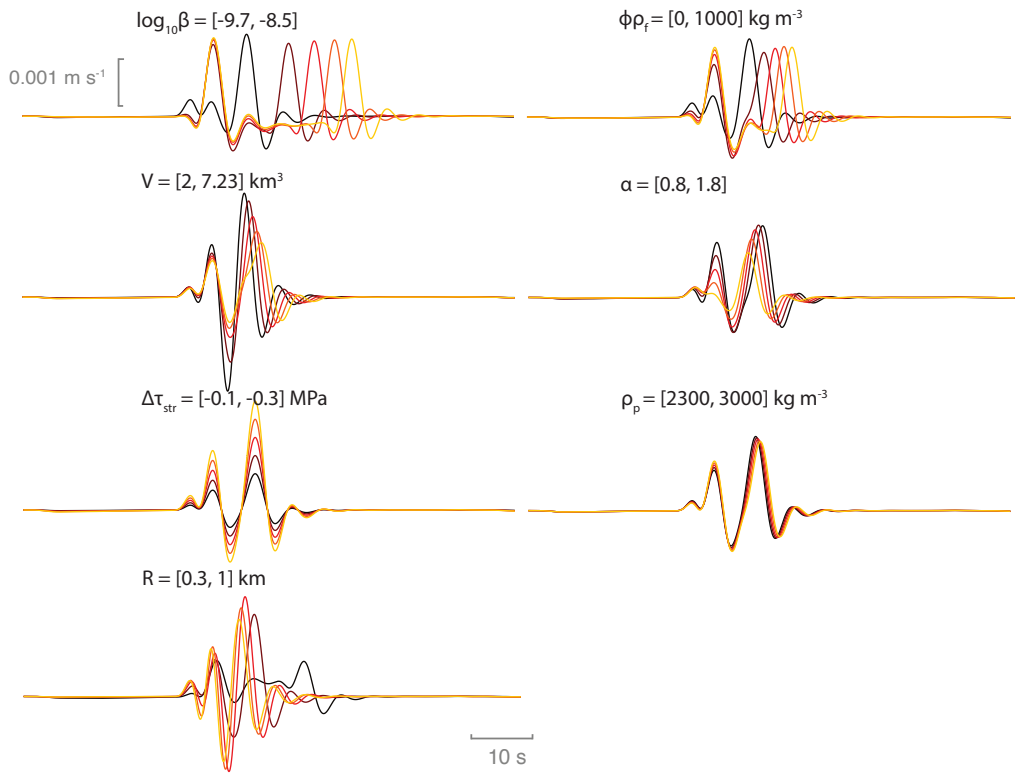

Figure S1: Sensitivity of simulated VLP waveforms to model parameters. Simulated vertical component velocity waveforms are shown with corresponding tested parameters. Values in brackets represent the lower and upper bounds of values tested. 5 evenly-spaced values are chosen within the bounds. Lighter color waveforms correspond to larger parameter values.

3 Velocity models of Kīlauea's summit

We opt to use a homogeneous half-space velocity model for computing synthetic seismograms. The reasoning is that common velocity models for Kīlauea's summit region (e. g. Lin et al., 2014) do not have fine enough resolution in the immediate proximity of the Halema'uma'u magma chamber. Thus, seismic velocity models of Kīlauea tend to overestimate the crustal shear modulus due to spatial averaging of low-velocity zones near the chamber with high-velocity zones much farther away. In the absence of higher-resolution velocity model, we use a constant shear modulus of 3 GPa (Anderson et al., 2019), density of 3000 $\mathrm{kg} \cdot \mathrm{m}^{-3}$, and a Poisson's ratio of 0.25 to compute for spatially uniform p and s wave velocities. At a period > 5 s, the VLP response is likely close to the quasi-static response of the earth, which justifies the low shear modulus used. Body wave scaling relationship indicates that increase μ decreases velocity waveform amplitude linearly, which biases estimated chamber pressure increase upwards. It is also shown that, although making the velocity below 3.5 km significantly faster (Fig. S2) elongates the simulated waveform in time (more pronounced in vertical component), the overall waveform shape does not change appreciably.

4 Validation of static limit deformation

The Eshelby solution for a moment tensor representing spheroidal cavities is derived in homogeneous full space (Eshelby, 1957). To ensure that the moment tensor is

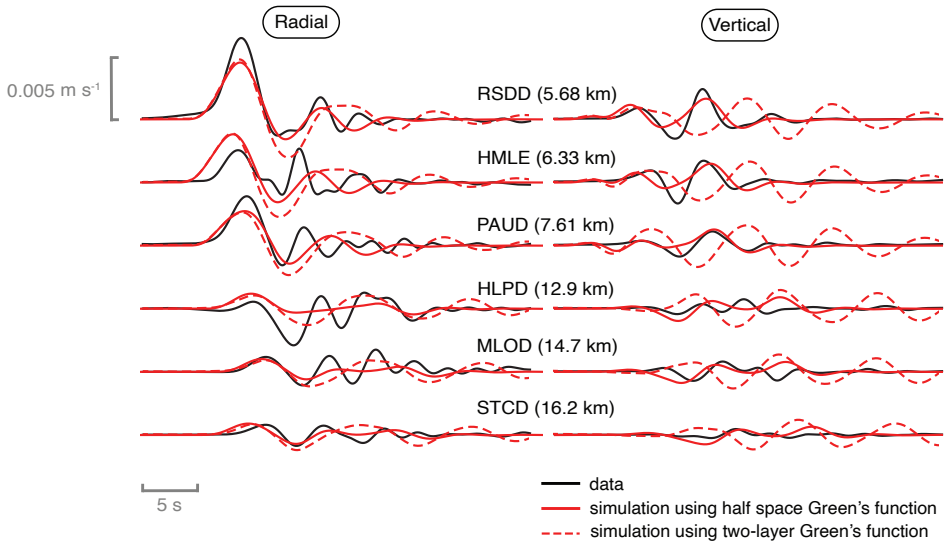

Figure S2: Comparing simulated waveforms with homogeneous half space model ($c_p = 1.73$ km/s and $c_s = 1$ km/s) and two layer model ($c_p = 1.73$ km/s and $c_s = 1$ km/s down to 3.5 km, below which $c_p = 5.5$ km/s and $c_s = 3.1$ km/s). At the stations' distances, adding a high velocity layer below 3.5 km elongates the simulated waveform in time.

adequate for centroid depths consistent with typical basaltic chambers, we compare the static deformation predicted using elasto-dynamic Green's functions with those predicted by the semi-analytical Yang-Cervelli model (Fig. S3). The results demonstrate that, for a large range of chamber aspect ratios, $0.2 - 1.4$, the Eshelby solution is adequate at a chamber centroid depth < 2.5 km.

5 Prior constraints

The characteristics of the simulated waveforms are dictated by both source dynamics and Green's functions, the latter of which are fixed to the assumed homogeneous velocity model. The dynamics of collapse is fully described by the dimensionless number π_0, and characteristic scales t^*, p^*, l^*. The simulated ground motions are also predicated on the crustal shear modulus μ, the Poisson's ratio, ν, and the chamber aspect ratio, α. A careful examination on the inter-dependence of the aforementioned parameters indicate that inverting the following parameters minimizes redundancy: $\Delta\tau_{str}$, V, β, ρ_p, $\phi\rho_f$, R, and α. In particular, the piston length, L, is not independent of chamber volume, V, and the chamber centroid depth, Δz: $L = \Delta z - (\frac{3V}{4\pi}\alpha^2)^{1/3}$, due to the assumption that the caldera block is directly situated above the chamber.

The choice of bounds on the uniform portion of Gaussian prior distributions is informed by previous studies. Surface expressions of the ring fault delineate a caldera block diameter varying between ~ 1.6 and 2.7 km. To account for uncertainties in subsurface ring fault geometry, we allow a prior range on ring fault radius, R, to vary between 0.5 and 1.3 km. The bulk density of typical basaltic rock in Hawaii averages at 2550 kg $\cdot$ m^{-3} (Moore, 2001), so we consider $\rho_p = 2400 - 2800$ kg $\cdot$ m^{-3}. The ratio $\phi = 1/3$ is the upper bound on the percentage of magma in the chamber contributing to the total inertia of the system. Assuming that typical basaltic magma density is ~ 2600 kg $\cdot$ m^{-3} and $\phi = 1/12 - 1/3$, we use an effective density of magma, $\phi\rho_f = 210 - 870$ kg $\cdot$ m^{-3}.

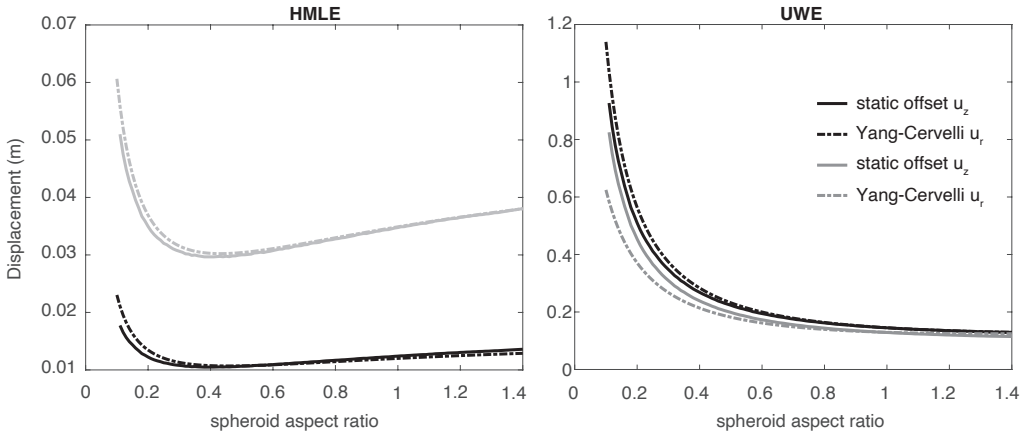

Figure S3: Simulated static surface displacements at various aspect ratios. left: (a) vertical and radial displacements at HMLE. (b) vertical and radial displacement at UWE. Vertical displacement in black; radial displacement in gray. Static limit of dynamic displacement in solid lines and Yang-Cervelli displacement in dashed lines. The results are computed with a pressure increase of 6.92 MPa, a chamber depth of 2.18 km, a chamber volume of 4 km^3, a crustal shear modulus of 3 GPa, and a Poisson's ratio of 0.25.

For the chamber volume, a 68% confidence interval, $V = 2.5 - 7.2$ km^3, estimated by Anderson et al. (2019), is used. We use a total reservoir compressibility of $\beta = 10^{-9.70} - 10^{-8.88}$ Pa^{-1}, where the upper bound is the upper 68% bound estimated by Anderson et al. (2019). Based on previous geodetic studies of the Halema'uma'u reservoir, the chamber is expected to be a near spherical body, with an aspect ratio of $\alpha = 1 - 1.4$.

Total shear strength drop can be estimated from the pressure increase in the chamber after each collapse:

$$|\Delta\tau_{str}| = \frac{1}{2}\frac{\pi R^2 \Delta p}{2\pi RL} = \frac{R\Delta p}{4L} \tag{4}$$

where the shear strength drop is half of the total drop in stress, in the full dynamic overshoot limit. Co-collapse pressure increase, Δp, has been estimated to be $1-3$ MPa (Segall et al., 2019). For a piston radius, $R = 500-1300$ m, and $L = 750-1200$ m, the shear strength drop needed to return the piston to static equilibrium is $0.1 - 1.3$ MPa.

6 Data covariance matrices

We assume that the data errors are normally distributed such that the likelihood function is:

$$P(\boldsymbol{d}|\boldsymbol{m}) = \prod_{i=GNSS,VLP} (2\pi)^{-N_i/2} det(\boldsymbol{C_i})^{-1/2} \times exp[-\frac{1}{2}(\boldsymbol{d_i} - \boldsymbol{G}(\boldsymbol{m}))^T \boldsymbol{C_i}^{-1}(\boldsymbol{d_i} - \boldsymbol{G}(\boldsymbol{m}))] \tag{5}$$

where the likelihood of both GNSS displacement offsets and VLP velocity waveforms are accounted for in the inversion. Here, N is the number of data points in each data set, $\boldsymbol{C}$ is the data covariance matrix, and $\boldsymbol{G}$ is the forward model operator.

The covariance matrices for both data sets are assumed to be diagonal (uncorrelated noise). GNSS uncertainties are propagated through stacking time series and differencing positions (Segall et al., 2020). VLP waveform uncertainties are set to a magnitude ensuring that, the weighted sum of squared residuals, $(\boldsymbol{d_i} - \boldsymbol{G}(\boldsymbol{m}))^T \boldsymbol{C_i}^{-1}(\boldsymbol{d_i} - \boldsymbol{G}(\boldsymbol{m}))$, is of order $N-M$, given a sampling rate (the weighted sum of square residuals follow a χ^2 distribution with $N-M$ degree of freedom, where N is the number of

data points and M is the number of estimated parameters). Such an approach ensures that the magnitude of data uncertainties are not significantly under- or over- estimated. To account for the large number of waveform data points versus GNSS static offset data points, a trial-and-error weight is applied to the likelihood for the static offsets.

7 Parameter correlations

By design, the inverted parameters are rather independent of each other, and thereby lack correlations (Fig. S4). There is a weak, positive correlation between chamber volume, V, and total compressibility, β, the reason of which may not be immediately clear, given the typical trade off between V and β in volumetric sources. However, such behavior is explained by noting the nonlinear dependence of the characteristic scales (Eqn. B1a - B1c) on V, given $m' = m + \phi\rho_f V$. The positive correlation between piston radius R, and β (or V) potentially explains the apparent small radii estimated from inversion.

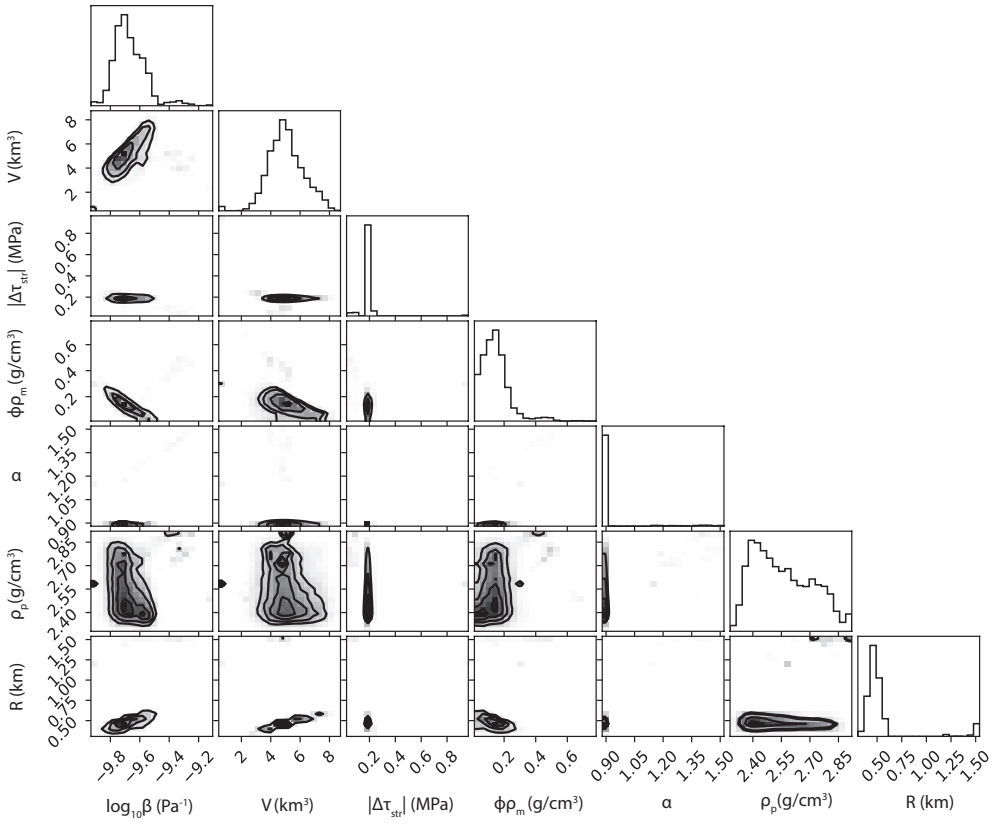

Figure S4: Correlation of inverted parameters. Parameters are mostly independent of each other, except chamber volume-compressibility and chamber volume-piston radius.

References

Anderson, K., Johanson, I., Patrick, M. R., Gu, M., Segall, P., Poland, M., ... Miklius, A. (2019). Magma reservoir failure and the onset of caldera collapse at Kīlauea volcano in 2018. *Science*, *366*(6470).

Eshelby, J. D. (1957). The determination of the elastic field of an ellipsoidal inclusion, and related problems. *Proceedings of the royal society of London. Series A. Mathematical and physical sciences*, *241*(1226), 376–396.

Lin, G., Shearer, P. M., Matoza, R. S., Okubo, P. G., & Amelung, F. (2014). Three-dimensional seismic velocity structure of Mauna Loa and Kīlauea volcanoes in Hawaii from local seismic tomography. *Journal of Geophysical Research: Solid Earth*, *119*(5), 4377–4392.

Moore, J. G. (2001). Density of basalt core from Hilo drill hole, Hawaii. *Journal of Volcanology and Geothermal Research*, *112*(1-4), 221–230.

Segall, P., Anderson, K., Johanson, I., & Miklius, A. (2019). Mechanics of inflationary deformation during caldera collapse: Evidence from the 2018 Kīlauea eruption. *Geophysical Research Letters*, *46*(21), 11782–11789.

Segall, P., Anderson, K., Pulvirenti, F., Wang, T., & Johanson, I. (2020). Caldera collapse geometry revealed by near-field GPS displacements at Kīlauea volcano in 2018. *Geophysical Research Letters*, *47*(15), e2020GL088867.